# Pd–Rh Nanocrystals with Tunable Morphologies and Compositions as Efficient Catalysts toward Suzuki Cross-Coupling Reactions

Si-Bo Wang,[‡] Wei Zhu,[‡] Jun Ke, Mu Lin, and Ya-Wen Zhang*

Beijing National Laboratory for Molecular Sciences, State Key Laboratory of Rare Earth Materials Chemistry and Applications, PKU-HKU Joint Laboratory in Rare Earth Materials and Bioinorganic Chemistry, and College of Chemistry and Molecular Engineering, Peking University, Beijing 100871, China

S *Supporting Information*
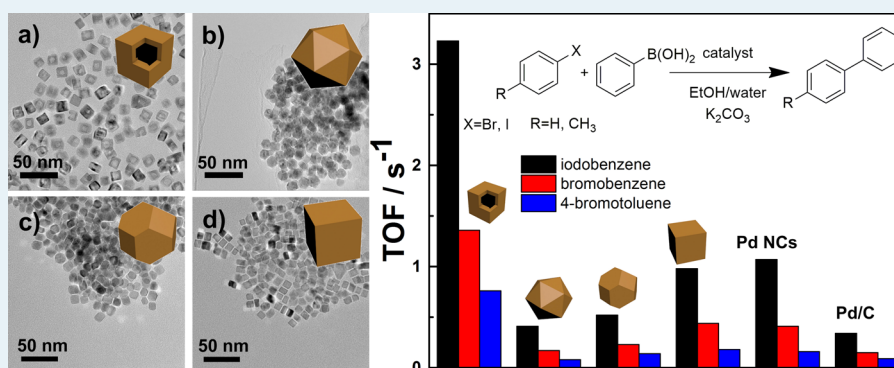
ABSTRACT: Delicate elaboration of the nanostructures of multimetal catalytic materials with well-defined shapes and compositions to reveal their potential use as heterogeneous nanocatalysts for organic synthetic reactions with the combined merits of heterogeneous and homogeneous catalysis is both scientifically and technologically important, but this type of investigation has remained rarely pursued. In this work, we demonstrated a facile hydrothermal approach toward the one-pot shape-selective syntheses of Pd–Rh nanocrystals with tunable compositions and morphologies, including hollow nanocubes (NCs), nanoicosahedrons (NIs), and nanotruncated octahedrons (NTOs), using poly(vinylpyrrolidone) as both reductant and capping agent and halide anions (Br⁻/I⁻) as shape control agents. The formation of Pd–Rh hollow NCs was induced by an iodine adsorbate-induced reconstruction mechanism with KI, whereas the formation of Pd–Rh NIs and NTOs were realized by controlling the selective nucleation of twinned seeds or single crystal seeds and their relative growth rates along different facets (e.g., (111) and (100) facets) through finely adjusting the Pd/Rh ratio and the amount of KBr added in the absence of KI. Due to the great significance of Pd-catalyzed organic reactions, the catalytic performances of Pd–Rh nanocrystals for Suzuki cross-coupling reactions with different reactants were evaluated. The measured turnover frequencies (TOFs) suggested that Pd–Rh hollow NCs held considerably enhanced catalytic activities (at least 3 times) than other Pd-based solid nanocrystals including Pd–Rh NIs, Pd–Rh NTOs, Pd–Rh NCs, Pd NCs, and commercial Pd/C, with iodobenzene as the reactant. In addition, even for more inert reactants such as bromobenzene or 4-bromotoluene, the catalytic activities of Pd–Rh hollow NCs were still impressive (showing similar TOFs to those of other shapes for reactions with iodobenzene as the reactant), indicating the promising application of Pd-based nanocatalysts for other powerful Pd-catalyzed organic synthesis reactions. Meanwhile, Pd-based solid NCs, enclosed with (100) facets only, showed better catalytic performance than NIs as well as NTOs, which had a larger fraction of (111) facets other than (100) ones, further suggesting that morphology differences were vitally significant to tune the catalytic performances of bimetallic nanocatalysts.

KEYWORDS: *Pd–Rh nanocrystals, bimetallic alloys, shape control, nanocatalysis, Suzuki cross-coupling reaction, heterogeneous catalyst*

INTRODUCTION

Because noble metal nanoparticles (NPs) demonstrate unique catalytic properties in electrochemical reactions,[1] gas-phase reactions,[2] and organic synthesis reactions,[3] they have wide applications in fuel cells, energy conversion, chemical manufacturing, environmental remediation, and so forth.[4] The development of highly active, selective, and durable noble metal nanocatalysts is vitally important for atomically utilizing the catalysts and the reactants with the maximum product output at low cost and low environment impact in the above chemical transformations for applications.

Traditionally, catalysis is divided into two categories—heterogeneous and homogeneous catalysis. Both of them hold their own reaction pathways, catalytic processing advantages, and

unique practical applications.[5] Compared to widespread applications in heterogeneous reactions including gas phase and electrocatalytic reactions, nowadays, nanocatalysts for traditionally homogeneous reactions, such as organic syntheses, have drawn great attention.[3,5b] The syntheses of complex organic molecules (e.g., pharmaceuticals, fine chemicals, and their corresponding intermediate compounds) through formation of aromatic carbon−carbon bonds via cross-coupling reactions with metal nanocatalysts have recently emerged with great importance because of facile separation of byproducts as well as low reagent toxicities endorsed by the highly efficient nanocatalysts.[3,6] Meanwhile, with the natural benefit of facile separation, nanocatalysts are promising to achieve the advantages of both homogeneous and heterogeneous catalytic reactions (i.e., high catalytic activities and selectivities, easy separation of products, and good recyclability of the catalysts). For such reactions, palladium holds a significant role, which is used in the form of Pd(0) with the presence of ligands resulting from higher catalytic activities despite their separation issues in catalytic processing. Recently, the actual active species for the Suzuki cross-coupling reaction, a kind of Pd-catalyzed organic reaction, are proved to be Pd(0) atoms on the surfaces of the catalysts,[7] which makes it possible to develop Pd-based nanocatalysts with comparable catalytic performance to homogeneous Pd catalysts for such reactions.

So far, the colloidal synthesis approach represents a robust strategy to tune the catalytic performances of the metal nanocatalysts via controlling the chemical composition, crystalline shape and size, oxidation states of metals, and metal segregation.[8] Due to promising chemical and physical properties including not only the combination of performances associated with different metals but also new capabilities resulting from the synergetic effect of metal constituents, bimetallic[9] or trimetallic[10] NPs showed greater significance than monometallic ones in wide applications. Moreover, recent studies have indicated that the construction and manipulation of nanostructures with well-defined morphologies such as cubes, octahedrons, tetrahedrons, and hierarchical (e.g., hollow, dendritic, etc.) structures[11] is a promising way to maximize the catalytic performances of the metal nanocatalysts by modulation of atom arrangement, electronic structures, and accessible active sites of the catalysts.[12] Though more difficult and complicated than syntheses of monometallic NPs, thanks to great efforts of many research groups, a myriad of methods have been developed for the controlled and designed preparation of bimetallic or trimetallic NPs to tailor their catalytic properties in past decades, such as faceted Pt−Ni NPs,[9d] Pd−Pt nanodendrites,[9e] dealloyed Pt−Cu core−shell nanostructures,[12a] Pt−Cu nanosheets as well as nanocones,[11f] trimetallic Pt₃Ni@M core−shell structures,[10b] and so on.

Recently, Pd−Rh NPs were shown to have excellent performance in wide applications such as hydrogen storage and as catalysts for organic synthetic reactions, electrocatalytic reactions, or gas phase reactions.[13] More importantly, the syntheses of bimetallic Pd−Rh nanocatalysts in various morphologies (i.e., especially those complicated ones) in order to tailor their properties have drawn considerable interest.[14] For instance, the Xia group prepared a variety of Pd−Rh nanocrystals with distinctive elemental distributions via a two-step approach.[14a,b] The Tsung group obtained Pd−Rh nanoboxes via the epitaxial overgrowth of Rh on Pd cubic seeds.[14c,d] Therefore, it is of great significance to develop a facile and efficient method to obtain Pd−Rh NPs with tunable compositions and shapes by delicate controlled synthetic chemistry, which is still a challenge so far.

In this article, we report the selective syntheses of Pd−Rh nanocrystals with various shapes and compositions, including hollow nanocubes (NCs), nanoicosahedrons (NIs), and nano-truncated octahedrons (NTOs), via a one-step hydrothermal approach with fine control of reaction conditions for each morphology. More importantly, considering the wide and significant applications of Pd-catalyzed organic synthesis reactions, the as-obtained Pd−Rh nanocrystals with tunable morphology and composition were utilized as nanocatalysts for Suzuki cross-coupling reactions with various reactants, including active ones and inert ones, and their catalytic performances were systemically evaluated as well as compared with commercial Pd/C catalyst as a reference.

■ EXPERIMENTAL SECTION

Chemicals. Palladium chloride (PdCl₂, analytical reagent (A.R.); Shenyang Research Institute of Nonferrous Metal, China), rhodium trichloride trihydrate (RhCl₃·3H₂O, A.R.; Sinopharm Chemical Reagent Co. Ltd., China), potassium bromide (KBr, A.R.; Sinopharm Chemical Reagent Co. Ltd., China), potassium iodide (KI, A.R.; Beijing Chemical Works, China), poly(vinylpyrrolidone) (PVP; M_w: ∼55 000; Sigma-Aldrich), sodium chloride (NaCl, A.R.; Sinopharm Chemical Reagent Co. Ltd., China), potassium carbonate (K₂CO₃, A.R.; Sinopharm Chemical Reagent Co. Ltd., China), iodobenzene (Tokyo Chemical Industry Co. Ltd.), bromobenzene (J&K Scientific, China), 4-bromotoluene (J&K Scientific, China), phenylboronic acid (Tokyo Chemical Industry Co. Ltd.), palladium on activated carbon (Pd/C, 30 wt % loading, Sigma-Aldrich), naphthalene (Beijing Chemical Works, China), biphenyl (Tokyo Chemical Industry Co. Ltd.), 4-methylbiphenyl (J&K Scientific, China), dichloromethane (A.R.; Beijing Chemical Works, China), acetone (A.R.; Beijing Chemical Works, China), ethanol (A.R.; Beijing Chemical Works, China). The water used in the syntheses was ultrapure (Millipore, 18.2 MΩ·cm).

Preparation of Na₂PdCl₄ Solution. Na₂PdCl₄ solution was prepared by mixing 1.0 g of PdCl₂ and 0.66 g of NaCl with 100 mL of H₂O at room temperature under stirring overnight.

Synthesis of Pd−Rh Hollow NCs. In a typical synthesis, a noble metal precursor solution (containing 0.03 mmol of PdCl₂, 0.06 mmol of RhCl₃·3H₂O, and 0.06 mmol of NaCl), PVP (100 mg), KBr (720 mg) and KI (1 mg) were dissolved in 15 mL of water, and the as-formed solution was then transferred to a 20 mL Teflon-lined stainless steel autoclave before sealing. After that, the autoclave was heated at 180 °C for 4 h before it was cooled to room temperature. The black nanoparticles were centrifuged with the addition of 50 mL of acetone and then washed with a mix of ethanol/acetone for several times.

Synthesis of Pd−Rh NIs. In a typical synthesis, a noble metal precursor solution (containing 0.06 mmol of PdCl₂, 0.03 mmol of RhCl₃·3H₂O, and 0.12 mmol of NaCl), PVP (100 mg), and KBr (720 mg) were dissolved in 15 mL of water, and the as-formed solution was then transferred to a 20 mL Teflon-lined stainless steel autoclave before sealing. After that, the autoclave was heated at 180 °C for 4 h before it was cooled to room temperature. The black nanoparticles were centrifuged at 5000 rpm for 5 min and then washed with a mix of ethanol/acetone for several times.

Synthesis of Pd−Rh NTOs. In a typical synthesis, a noble metal precursor solution (containing 0.06 mmol of PdCl₂, 0.03 mmol of RhCl₃·3H₂O, and 0.12 mmol of NaCl), PVP (100 mg), and KBr (1440 mg) were dissolved in 15 mL of water, and the as-formed solution was then transferred to a 20 mL

Teflon-lined stainless steel autoclave before sealing. After that, the autoclave was heated at 180 °C for 4 h before it was cooled to room temperature. The black nanoparticles were centrifuged with addition of 50 mL of acetone and then washed with a mix of ethanol/acetone for several times.

Synthesis of Pd NCs. In a typical synthesis, a noble metal precursor solution (containing 0.09 mmol of $PdCl_2$, and 0.18 mmol of NaCl), PVP (150 mg), and KBr (360 mg) were dissolved in 15 mL of water, and the as-formed solution was then transferred to a 20 mL Teflon-lined stainless steel autoclave before sealing. After that, the autoclave was heated at 180 °C for 4 h before it was cooled to room temperature. The black nanoparticles were centrifuged with addition of 50 mL of acetone and then washed with a mix of ethanol/acetone for several times.

Synthesis of Pd−Rh Solid NCs. In a typical synthesis, a noble metal precursor solution (containing 0.06 mmol of $PdCl_2$, 0.03 mmol of $RhCl_3 \cdot 3H_2O$, and 0.12 mmol of NaCl), PVP (200 mg), and KBr (1080 mg) were dissolved in 15 mL of water, and the as-formed solution was then transferred to a 20 mL Teflon-lined stainless steel autoclave before sealing. After that, the autoclave was heated at 180 °C for 4 h before it was cooled to room temperature. The black nanoparticles were centrifuged with addition of 50 mL of acetone and then washed with a mix of ethanol/acetone for several times.

Synthesis of $Pd_{0.32}Rh_{0.68}$ Solid NCs for Etching Procedure. In a typical synthesis, a noble metal precursor solution (containing 0.03 mmol of $PdCl_2$, 0.06 mmol of $RhCl_3 \cdot 3H_2O$, and 0.06 mmol of NaCl), PVP (100 mg), and KBr (720 mg) were dissolved in 15 mL of water, and the as-formed solution was then transferred to a 20 mL Teflon-lined stainless steel autoclave before sealing. After that, the autoclave was heated at 180 °C for 4 h before it was cooled to room temperature. The black nanoparticles were centrifuged with addition of 50 mL of acetone and then washed with a mix of ethanol/acetone for several times.

Procedure to Etch $Pd_{0.32}Rh_{0.68}$ Solid NCs. In a typical synthesis, as-washed $Pd_{0.32}Rh_{0.68}$ solid NCs (9 mg), PVP (100 mg), and KI (1 mg) were dissolved in 15 mL of water, and the as-formed solution was then transferred to a 20 mL Teflon-lined stainless steel autoclave before sealing. After that, the autoclave was heated at 180 °C for 2 h before it was cooled to room temperature. The black nanoparticles were centrifuged with addition of 50 mL of acetone and then washed with a mix of ethanol/acetone for several times.

Instrumentation. Samples for transmission electron microscopy (TEM), high resolution TEM (HRTEM), energy dispersive X-ray spectroscopy (EDS) analysis, high-angle annular dark field scanning transmission electron microscopy (HAADF-STEM), HAADF-STEM-EDS line scans and HAADF-STEM-EDS element mapping were prepared by drying a drop of diluted Pd−Rh NPs on copper grids. All the observations mentioned above were performed on a FEG-TEM (JEM-2100F, JEOL, Japan) operated at 200 kV. Inductively coupled plasma-atomic emission spectroscopy (ICP-AES) analysis was performed on a Profile Spec ICP-AES spectrometer (Leeman, U.S.). The powder X-ray diffraction (PXRD) patterns of Pd−Rh NPs were obtained on a Rigaku D/MAX-2000 diffractometer (Japan) with a slit of 1/2° at a 2θ scan rate of 4°·min^{-1} under Cu Kα radiation (λ = 1.5406 Å). The X-ray photoelectron spectroscopy (XPS) results of the NPs were obtained on an Axis Ultra Imaging Photoelectron Spectrometer (Kratos Analytical Ltd., U.K.). NPs dispersed in ethanol were previously dropped on silicon wafers for the preparation of XPS measurements. Gas-chromatography (GC) analysis was performed on an Agilent 7890A GC

(Agilent Technologies, U.S.). Column: J&W DB-5 ms, 30 m × 250 μm, 0.5 μm. Temperature: The initial temperature is 60 °C, and then it is increased 10 °C/min to 200 °C. After that, the oven was kept at 200 °C for 5 min and at 250 °C for 1 min. Retention Time: 8.8 min for naphthalene, 11.5 min for biphenyl, and 13.0 min for 4-methylbiphenyl.

Suzuki Cross-Coupling Reaction Studies. The coupling between phenylboronic acid and aryl halide (iodobenzene, bromobenzene, or 4-bromotoluene) was performed according to a previous report.[3b] Aryl halide (iodobenzene, bromobenzene, or 4-bromotoluene, 0.3 mmol) was added into ethanol (4 mL) with phenylboronic acid (0.073 g, 0.6 mmol), K_2CO_3 (0.138 g, 1 mmol), and nanocatalyst (containing 50 μg noble metal NPs for iodobenzene or bromobenzene as reactants, and 100 μg for 4-bromotoluene as the reactant). The mixture was kept in an oil bath at 85 °C for 20 min under magnetic stirring. Then naphthalene (0.038g, 0.3 mmol) was added as the reference. After that, the product was extracted with CH_2Cl_2 and analyzed by gas chromatography. The reaction was carried out three times under the same conditions for each catalyst.

Recycling Performance for Suzuki Cross-Coupling Reactions. The mixture was prepared in three flasks named A, B, and C, according to the procedure above. A was kept at 85 °C for 20 min, B was processed twice, and C was processed three times with the same procedure of A (i.e., kept at 85 °C for 20 min). Compared to Pd atoms leached into solutions, those at the surface of NPs were much more catalytically active,[7] and TOFs of the last 20 min were appropriate to measure the recycling performance.[6a]

■ RESULTS AND DISCUSSION

Syntheses and Characterizations of Pd−Rh Hollow NCs, Pd−Rh NIs, and Pd−Rh NTOs. Hollow NCs, NIs, and NTOs of Pd−Rh with various compositions can be prepared through the above described hydrothermal method, with high shape selectivities and narrow size distributions.

As shown in the transmission electron microscopy (TEM) image (Figure 1a), hollow Pd−Rh NCs were obtained with a narrow size distribution (ca. 14.4 ± 0.6 nm, Figure S1) and a high shape selectivity (ca. 95%). The light contrast in the center of Pd−Rh NCs (Figure 1a,b) demonstrated that Pd−Rh NCs held hollow structures, as also confirmed by HAADF-STEM image (Figure 1c). HRTEM image and corresponding fast Fourier transformation (FFT) pattern confirmed that the NCs were enclosed by six (100) facets. The PXRD pattern (Figure S2) showed the formation of the face-centered-cubic (fcc)-structured Pd−Rh NCs with the calculated lattice constant of 0.3834(2) nm. EDS and ICP-AES both showed that the Pd/Rh ratio was around 1:2, equal to that in the metal precursors added in the synthesis. Moreover, HAADF-STEM-EDS line scan profile and element mapping results (Figure 1d and Figure S3) suggested a nearly homogeneous distribution of Pd and Rh atoms in the NCs.

As illustrated in TEM and HRTEM images (Figure 2a−d), Pd−Rh NIs obtained with a size of 16.3 ± 0.7 nm (Figure S4a) and a selectivity of 85% were bounded with 20 (111) facets, which were confirmed by distinctly observed (111)-twinned boundaries and FFT patterns as well. Through comparing 2-, 3-, and 5-fold symmetry HRTEM lattice fringes of the quasi-sphere Pd−Rh NPs (Figure 2b−d) with HRTEM simulations of gold NIs reported previously,[15] the structure of Pd−Rh NIs was confirmed. Furthermore, the HAADF-STEM-EDS line-scan profile (Figure 2e) suggested that unlike Pd−Rh hollow NCs, Pd−Rh NIs held a Pd@Rh core−shell structure.
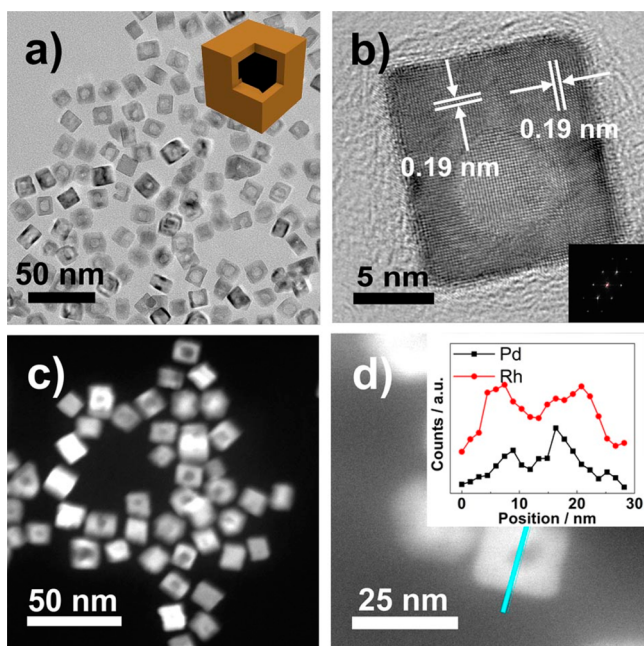
Figure 1. (a) TEM image (inset shows the geometric model), (b) HRTEM image (inset is the corresponding FFT pattern), (c) HAADF-STEM image, and (d) HAADF-STEM-EDS line-scan profile of Pd–Rh hollow NCs.

According to the corresponding PXRD pattern (Figure S2), Pd–Rh NIs were in the fcc structure with the calculated lattice constant of 0.3877(3) nm. Both EDS and ICP-AES results indicated that the Pd/Rh ratio in Pd–Rh NIs (ca. 2:1) was equal to that in the metal precursors added in the synthesis.

Compared to synthetic conditions of Pd–Rh NIs, Pd–Rh NTOs were obtained when the amount of KBr increased. According to TEM and HRTEM images (Figure 2f,g), with a high selectivity (90%), Pd–Rh NTOs were prepared in a size of 12.1 ± 0.9 nm (Figure S4b). As confirmed by both EDS and ICP-AES results, the Pd/Rh ratio in Pd–Rh NTOs was similar to that in metal precursors of the synthetic condition (ca. 2:1). PXRD pattern (Figure S2) suggested that Pd–Rh NTOs held the fcc structure with the calculated lattice constant of 0.3855(4) nm. Additionally, the HAADF-STEM-EDS line-scan profile (Figure 2h) showed that the distribution of Pd and Rh in NTOs was nearly homogeneous.

Conditions for Forming Pd–Rh Hollow NCs. To map the formation process of the Pd–Rh NPs with various morphologies and compositions, several factors including Pd/Rh ratio, elemental distribution, and shape evolution were monitored during the synthesis.

In the first hour of the reaction to obtain Pd–Rh hollow NCs, 75% of Pd(II) and 30% of Rh(III) were reduced (Figure 3a) due to the higher electrode potential of Pd(II)/Pd ($\varphi^0(PdBr_4^{2-}/Pd)$ = 0.563 V) than that of the Rh(III)/Rh pair ($\varphi^0(RhBr_4^{-}/Rh)$ = 0.411 V). As the reaction went on, the Pd/Rh ratio in the NPs decreased from 56:44 at 1 h to 29:71 at 8 h (Figure 3b). As illustrated in Figure 4a, incomplete solid NCs formed in 1 h. Then, hollow cubic shape appeared at 2 h (Figure 4b). Prolonging reaction time resulted in a higher selectivity of well-defined hollow NCs (Figure 4c,d). According to the HAADF-STEM-EDS line-scan profiles (Figure 1d and Figure S5), the as-obtained NPs held the structure with Pd-rich core and Rh-rich shell in the first 2 h. After that, by maintaining the composition (Figure 3b) and cubic shape, those NPs turned hollow. Meanwhile, possibly
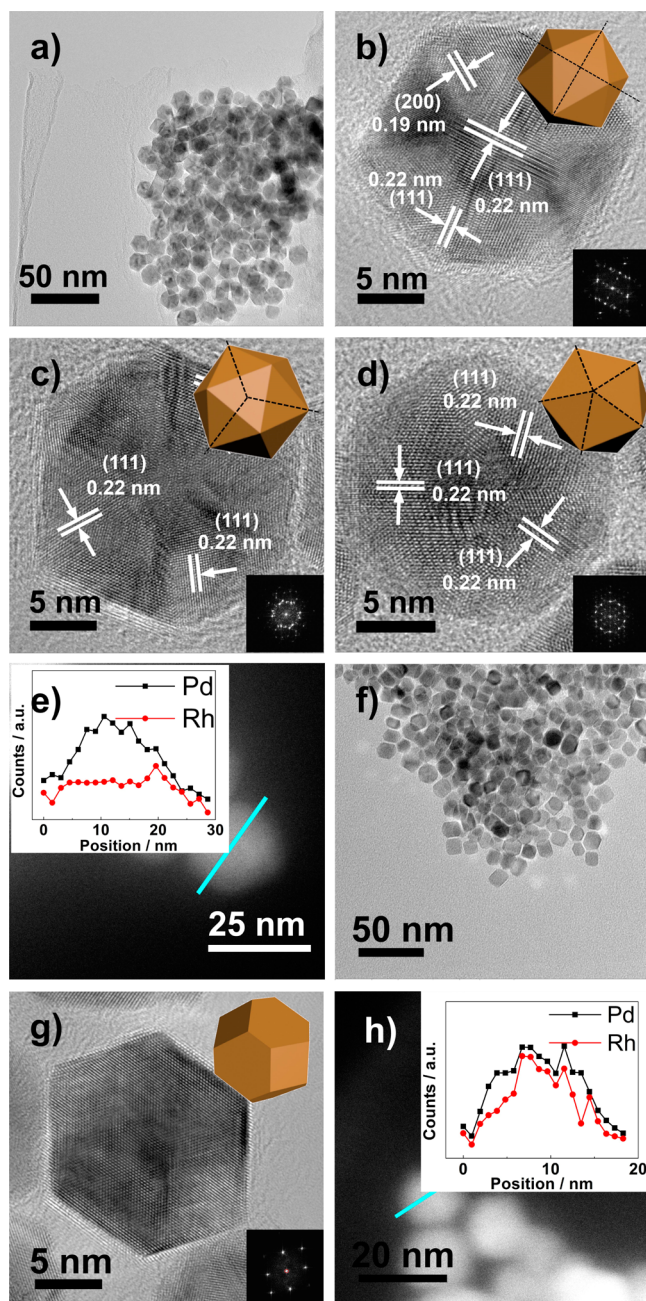

Figure 2. (a) TEM image, (b)–(d) HRTEM images (insets are corresponding FFT patterns and geometrical models with 2-, 3-, and 5-fold symmetries), (e) HAADF-STEM-EDS line-scan profile of Pd–Rh NIs, (f) TEM image, (g) HRTEM image (inset is corresponding FFT pattern and geometrical model), and (h) HAADF-STEM-EDS line-scan profile of Pd–Rh NTOs.

due to low lattice mismatch between Pd and Rh (ca. 2% in lattice constant),[16] the diffusion between core and shell occurred to acquire the nearly homogeneous element distribution of Pd and Rh for the NCs (Figure S3 and S5).

The synthesis of $Pd_{0.32}Rh_{0.68}$ hollow NCs was also tested at different temperatures. NCs synthesized at 160 and 200 °C held a similar morphology and composition with those obtained at 180 °C (Figure S6, and Table S1). Furthermore, Pd–Rh hollow NCs were observed at 140 °C when reaction time was prolonged to 24 h (Figure S7). Low temperature could slow down the reaction process, making it possible to distinguish the NCs
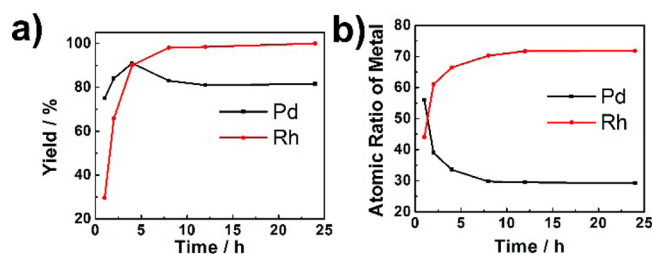
Figure 3. (a) Yields (utilizing ICP-AES to determine the amount of NPs) of Pd and Rh in the synthesis of Pd−Rh hollow NCs and (b) atomic ratios (ICP-AES results) of Pd and Rh in Pd−Rh hollow NCs taken at different growth stages during synthesis.
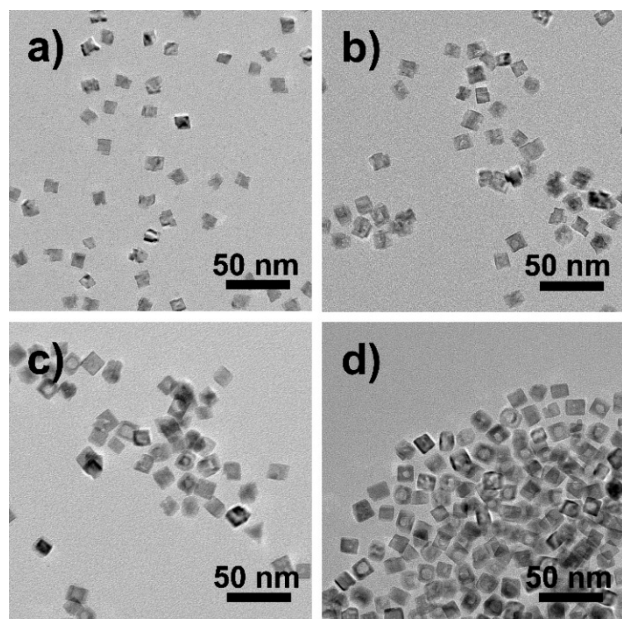

Figure 4. TEM images of Pd−Rh hollow NCs taken at various reaction times: (a) 1 h, (b) 2 h, (c) 8 h, and (d) 24 h.

growth stages at 140 °C. As demonstrated by TEM images (Figure S6a and Figure S7) and ICP-AES results (Figure S8), formation of Pd-rich solid cubes (Pd/Rh = 83:28) occurred at first, and then they turned into incomplete solid NCs with Rh-rich shell by epitaxial growth on multisites of Pd-rich cubes. Subsequently, the etching of cores started, and the incomplete intermediates grew into perfect cubes. Finally, Pd−Rh hollow NCs were obtained after 1 day.

Without halide ions of Br⁻ and/or I⁻, neither hollow structure nor cubic shape was obtained (Figure S9), indicating that they played important roles in the construction of hollow cubic shape. TEM images of Pd−Rh NPs synthesized with various amounts of KBr (Figure 1a and Figure S10) suggested that Br⁻ ions seldom participated in the hole-forming process. Only small irregular NPs were acquired without KBr, whereas quadrupling the amount of KBr compared to that in the typical synthesis resulted in aggregation of NPs. Considering that Br⁻ ions could be selectively adsorbed on the (100) facets of Rh and Pd NPs,[17] they should facilitate the formation of a cubic shape in our Pd−Rh NCs. Changes in quantities of KI brought about various degrees of etching (Figure 1a and Figure S11). Only solid Pd−Rh NCs were obtained without KI; however, cubes with different sizes formed when 4-fold KI was added. When the range was changed from 0.5 mg to 2 mg (i.e., half to twice the amount) of I⁻ ions, Pd−Rh hollow NCs with different hole sizes were acquired.

Previously, it was demonstrated that iodine adsorbed on Pd surfaces could induce dissolution of Pd atoms,[18] and I⁻ ions were vulnerable to be oxidized to iodine due to the existence of oxygen in this synthesis ($\varphi^0(I_2/I^-) = 0.621$ V, $\varphi^0(O_2/H_2O) = 1.229$ V). Hence, I⁻ ions were essential for the etching process to form hollow structures in this work. Further, the corrosion of Pd−Rh solid NCs with I⁻ ions was tested. After the hydrothermal treatment, TEM images (Figure S11a and S12) showed that Pd−Rh solid NCs became rough and porous with a slight decrease of Pd content from 33% to 29%. Meanwhile, the Pd and Rh contents in the solution after the hydrothermal reaction were examined, and it indicated that very little Rh was detected (less than the detection limit). However, there was much more Pd left in the solution (ca. 0.3 mg), suggestive of a significant etching effect on Pd instead of Rh from the as-formed nanocrystals by iodine etchant. In addition, it was noted that hollow NCs could be obtained only when Pd precursors were added (Figure S13). Moreover, according to XPS results, the amounts of I⁻ and Br⁻ were almost the same (Br/I = 1:1.2, Figure 5) on the surfaces
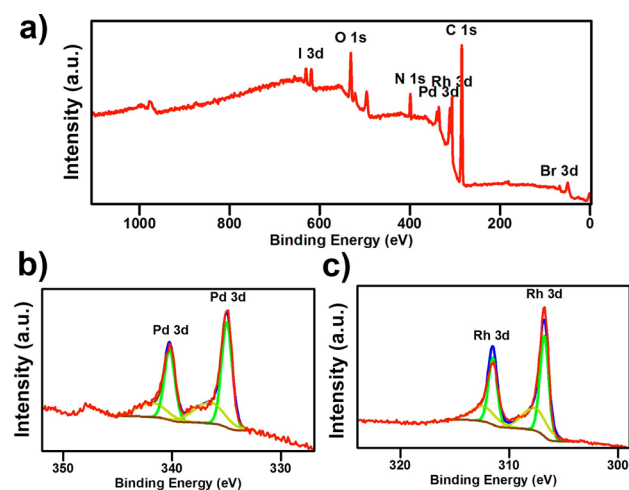

Figure 5. XPS spectra of Pd−Rh hollow NCs. (a) Survey spectra, (b) Pd 3d spectra fitted as the linear combination of Pd(0) and Pd(II) 3d spectra (brown line: background; red dots: experimental data; blue line: fitted data; green line: fitting curve for Pd(0); yellow line: fitting curve for Pd(II)), and (c) Rh 3d spectra fitted as the linear combination of Rh(0) and Rh(III) 3d spectra (brown line: background; red dots: experimental data; blue line: fitted data; green line: fitting curve for Rh(0); yellow line: fitting curve for Rh(III)).

of the NCs, despite the huge gap between their quantity of precursors added (720 mg of KBr to 1 mg of KI), and a portion of metal atoms on the surface layers were in high oxidation states (ca. 25% of Pd and 35% of Rh, Figure 5b,c), indicating a rather strong affinity and oxidation etching effect of iodine to the surface atoms of the NPs. Therefore, it was considered that the iodine adsorbate-induced reconstruction should account for the dissolution of Pd atoms in the NCs, as also suggested by the yield decrease of Pd from 91% to 83% in the ICP-AES results (Figure 3a).

The iodine adsorbate-induced reconstruction mechanism for the formation of the $Pd_{0.32}Rh_{0.68}$ hollow NCs was illustrated in Scheme 1. The NCs growth could be divided into three stages: generating Pd-rich cubes, forming incomplete NCs with Rh shell, and then turning into hollow structures. First, the reduction of Pd(II) occurred to form small Pd-rich cubes due to higher reduction potential of Pd(II) and selective adsorption of Br⁻ ions.

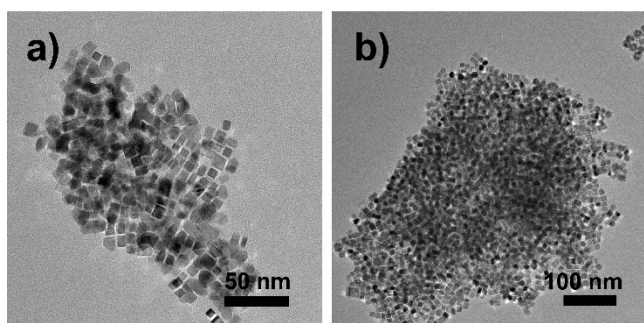**Scheme 1. Proposed Formation Process of Pd−Rh Hollow NCs**
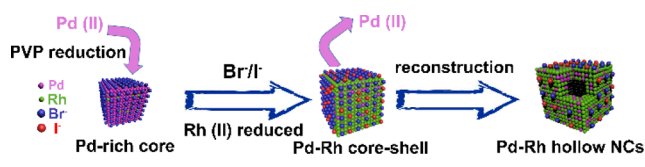
Then, Rh(III) was reduced to form Rh-rich shells. Later on, iodine adsorbate-induced reconstruction occurred to etch Pd core under hydrothermal treatment in the presence of O_2, and NCs turned nearly homogeneous resulting from the interdiffusion of Pd and Rh atoms between core and shell. Meanwhile, because of the selective adsorption of Br$^-$ ions on the (100) facets of Pd−Rh NPs, the shape finally turned into perfect cubes. By following this route, $Pd_xRh_{1−x}$ hollow NCs with other compositions could be obtained (Table S2 and Figure S13).

Conditions for Forming Pd−Rh NIs and Pd−Rh NTOs. Compared with Pd−Rh hollow NCs, Pd−Rh NIs were obtained when the ratio of Pd/Rh was increased to 2:1 or higher in the absence of KI. The effect of Pd/Rh ratio on the synthesis was first evaluated. According to the TEM images (Figure S14), proper Pd/Rh ratio (2:1 or higher, i.e., Pd-rich) was essential for the generation of twinned seeds of Pd−Rh NIs. Additionally, all the twinned NPs were observed to disappear with a small amount of KI added, just like the case for the shape evolution in forming Pd−Rh hollow NCs (Figure S13a). This result strongly suggested that the removal of twinned seeds would occur by the etching effect with halide ions/oxygen pairs.[19] Therefore, it was again proved that I$^-$ played a significant role in the present syntheses of Pd−Rh NPs with tunable morphologies.

The synthetic conditions of Pd−Rh NTOs and NIs were similar but with different amounts of KBr added. To rule out the possibility that NTOs were intermediates to form NCs, we examined the formation process of NTOs obtained with various reaction times. The shape of Pd−Rh NTOs changed little as the reaction time shifted (Figure S15) from 2 to 24 h, indicating that the Pd−Rh NTOs were thermodynamically favored products instead of the intermediates of NCs. Generally speaking, there were two major effects of Br$^-$ in the syntheses: selective adsorption onto the (100) facet of Pd−Rh so as to retard its growth rate and coordination with Pd(II) as well as Rh(III) to form more stable complexes in bringing about lower reduction rates of metal ions.[20] Moreover, a smaller amount of KBr resulted in NCs (Figure 6a) or NIs (Figure 2a), and double amounts of PVP (serving as the reductant in the syntheses) gave rise to NCs

as well under a faster growth rate obtained in this condition (Figure 6b). Thus, a slower growth rate was likely to favor for the formation of Pd−Rh NTOs.[20c] Due to lower surface energy of (111) facets,[21a] different from NCs as kinetic products, NTOs were more likely thermodynamic ones. Additionally, with a huge amount of KBr existing, the deposition rate was much smaller than the diffusion rate, resulting in the morphology turning into NTOs.[21b] Besides, the coordination ability to Pd(II) and Rh(III) as well as the selective adsorption capability of Br$^-$ could help the formation of single crystal seeds exposing (100) facets,[21] accounting for the disappearing of twinned NPs when a huge amount of KBr was added. In addition, Pd−Rh NTOs could be obtained with different Pd/Rh ratios (e.g., $Pd_{0.67}Rh_{0.33}$ and $Pd_{0.31}Rh_{0.69}$), and the sole use of either Pd or Rh precursors brought about NPs in other shapes (Figure S16), suggesting the important role of the coreduction of Pd(II) and Rh(III) in obtaining NTOs.

Synthetic Pathways for Pd−Rh NPs with Various Shapes. On the basis of the above experiment results and our understanding of the relationship between synthetic conditions and morphologies of the as-obtained Pd−Rh NPs, the synthetic pathways for the present shape- and composition-tunable syntheses of Pd−Rh nanocrystals were proposed in Scheme 2.

Scheme 2. Schematic Synthetic Diagram for Pd−Rh NPs with Various Morphologies
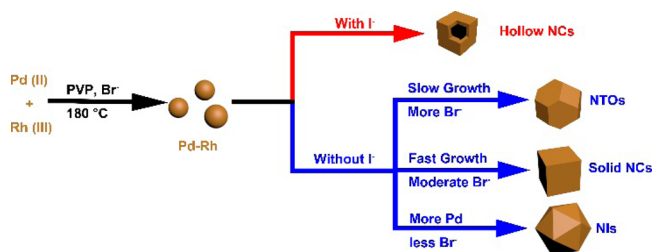
In the synthetic process of Rh−Pd nanocrystals, Pd(II) and Rh(III) precursors were reduced by PVP with the coexistance of KBr. We also observed three main factors strongly affecting the morphology of Pd−Rh NPs as obtained: the presence or absence of iodide ions, the growth rate of the NPs, and Pd/Rh ratio of metal precursors. With mere KI added, all seeds were single crystals that turned into Pd−Rh hollow NCs eventually due to iodide adsorbate-induced reconstruction effect as well as etching effect for twinned seeds.[18]

Without iodide ions, according to different amounts of KBr and Pd/Rh ratios, Pd−Rh solid NCs, NIs, and NTOs could be obtained under varied conditions. Resulting from its strong coordination ability to Pd(II) and Rh(III), KBr added showed an obvious effect on reducing the nucleation and growth rate of NPs.[20] Meanwhile, the lower surface energy of (111) facets than (100) facets and selective adsorption of KBr onto the {100} facets resulted in NCs as kinetic products preferably under a fast growth rate, and NTOs as partially thermodynamic products were preferred under a slow growth rate.[20c,21] Furthermore, with a huge amount of KBr employed in the synthesis, Pd−Rh NTOs would be formed under greatly retarded growth rate of NPs, whereas the use of a moderate amount of KBr would result in the formation of Pd−Rh solid NCs. Pd−Rh NIs were obtained under a small amount of KBr added and a sufficiently higher Pd content, due to the fact that the existence of excessive KBr in the synthesis could block the generation of twinned seeds[21] and that higher Pd/Rh ratios facilitate the formation of the twinned structure.

Figure 6. TEM images of Pd−Rh NCs synthesized with (a) 1080 mg KBr added and (b) 200 mg PVP added. All the other conditions were the same as those of Pd−Rh NTOs.

Catalytic Activities for Suzuki Cross-Coupling Reactions. Because Pd NPs are promising catalysts for Suzuki cross-coupling reactions,[3] catalytic performances of the Pd—Rh NPs with different compositions and morphologies were tested for this reaction with various reactants (Figure 7). Very little
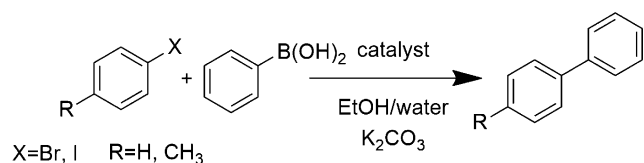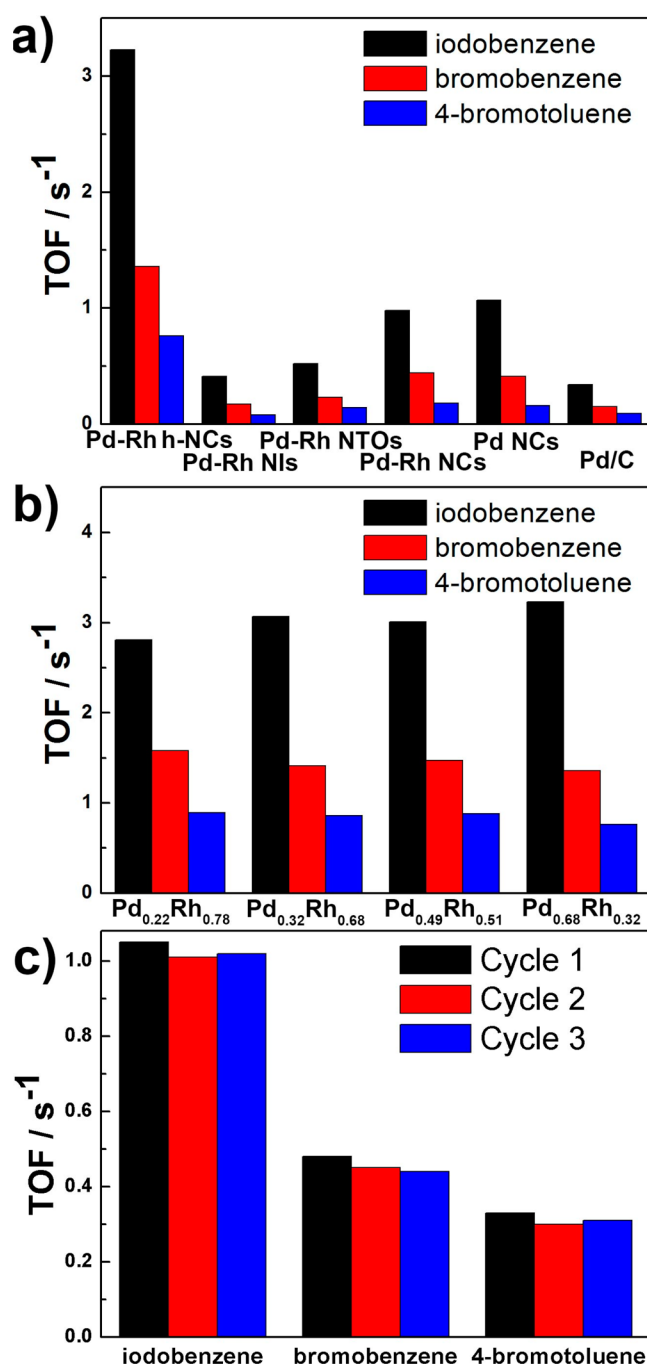
Figure 7. Suzuki cross-coupling reaction between aryl halide (iodobenzene, bromobenzene, or 4-bromotoluene) and phenylboronic acid used in the present work was utilized to evaluate catalytic activities of nanocatalysts.

biphenyl (yielding less than 1%) was detected in the absence of catalysts or utilizing Rh NCs (Figure S13f) as catalyst, indicating the unique catalytic activity of Pd atoms for Suzuki reactions. The intrinsic TOF of different nanocatalysts (defined as the product formation per surface Pd atom per second, Figure 8a,b, Table S3, and Table S4) for Suzuki reactions with iodobenzene as the reactant suggested that, compared to solid Pd-based NPs (i.e., Pd NCs, commercial Pd/C, Pd—Rh solid NCs (Figure S17), Pd—Rh NIs, and Pd—Rh NTOs), Pd—Rh hollow NCs with various compositions had significantly enhanced catalytic activities for Pd sites (ca. 3 s^{-1} for Pd—Rh hollow NCs and around 1 s^{-1} or lower for other solid NPs). Compared to Pd NCs, Pd—Rh solid NCs showed similar catalytic performance, whereas NIs and NTOs seemed less active as a catalyst for Suzuki reactions. In addition, catalytic performances of both Pd—Rh hollow NCs and solid NCs seemd irrelevant to the Pd/Rh raio (Figure 8b, and S18). Therefore, the morphology rather than composition held a stronger effect on the catalytic performances of the as-synthesized Pd—Rh nanocatalysts.

Given that oxidative addition is the rate-determining step of Suzuki reaction and it preferred Pd atoms prone to be oxidized[6b] and that XPS results suggested the distributions of metals (Pd or Rh) in various oxidation states on the surface of different Pd—Rh nanocrystals were almost the same (Table S5), higher TOF values for the Pd—Rh hollow NCs resulted from Pd atoms inclined to be oxidized due to their complicated morphology. That is, the rich kink and step sites on the inner rough faces of the hollow structures resulted in the higher energy of Pd atoms and made them prone to be oxidized.[3]

Moreover, considering solid NCs enclosed by six (100) facets, NTOs enclosed by a mixture of eight (111) and six (100) facets, and NIs enclosed by 20 (111) facets, higher catalytic activities of solid Pd and Pd—Rh NCs than NIs as well as NTOs suggested that (100) facets were likely more active compared to (111) facets. Additionally, although the reactants, aryl bromides and aryl halides with electron-donating groups were usually inert,[6b] the Pd—Rh hollow NCs could more actively initiate the oxidative addition step of the strong C—X bond rather than other solid NPs. The TOF values were at least triple for bromobenzene and 5-fold for 4-bromotoluene compared to other solid Pd-based NPs. Furthermore, the recycling capability of Pd$_{0.32}$Rh$_{0.68}$ hollow NCs was examined, and TOF values changed little within three cycles for the Pd$_{0.32}$Rh$_{0.68}$ hollow NCs (Figure 8c).

Similar results have been reported in the supported Pd nanocrystals, resulting from (100) facets of Pd nanoparticles that held a lower surface atom density and more coordinative unsaturation

Figure 8. (a) TOFs per surface Pd atom for Suzuki cross-coupling reaction with Pd—Rh hollow NCs (h-NCs), Pd—Rh solid NCs, Pd—Rh NIs, Pd—Rh NTOs, Pd solid NCs, and commercial Pd/C, (b) TOFs per surface Pd atom for Suzuki cross-coupling reaction with Pd—Rh hollow NCs in various Pd/Rh ratios, and (c) recycling performance of Pd$_{0.32}$Rh$_{0.68}$ hollow NCs for Suzuki cross-coupling reactions.

than (111) facets (surface atom density of Pd (100) and (111) atoms were $2/a^2$ and $2.3/a^2$, respectively, and unsaturated coordination number of Pd (100) and (111) atoms were 4 and 3, individually).[22] Given that both Pd and Rh held the fcc structure with similar lattice constants (0.389 and 0.380 nm for Pd and Rh, respectively) and that Pd—Rh nanoparticles held nearly homogeneous distribution of Pd and Rh atoms, the unsaturated coordination number was a persuasive way to explain the as-observed catalytic activity differences for the as-synthesized

Pd−Rh nanocrystals in different shapes. Thus, for the Pd−Rh nanocatalysts in Suzuki reactions, the higher TOFs were possibly due to the fact that they could adsorb more reactant molecules and more efficiently break the C—X bonds, which could be explained through differences in surface atom density and coordinate unsaturation of various facets.[22] Besides, probably resulting from defective (111) twin planes which could create more active sites for NIs,[23] Pd−Rh NIs enclosed by only (111) facets held similar catalytic performance with NTOs enclosed by both (111) and (100) facets.

Recently, it was reported that many solid catalysts for catbon−carbon bond-forming reactions developed thus far were actually homogeneous (i.e., their catalytic properties resulted from leached Pd). This elusive topic has drawn great interest and requires a full investigation.[24] In order to investigate the leaching issue of our Pd−Rh nanocatalysts, morphology and composition changes of the nanoparticles after Suzuki reactions were examined. According to the HRTEM images of nanocrystals after catalyzing the reaction (Figure S19), the morphology of Pd−Rh solid nanocrystals (solid NCs, NIs, and NTOs) changed slightly, and Pd−Rh hollow NCs changed a little more, while Pd NCs totally turned into other shapes. Meanwhile, ICP-AES results (Figure S20) indicated that Rh was leached little for all the samples, probably due to its inert catalytic activity to the Suzuki reactions, and compared to Pd NCs (ca. 20% loss in Pd), Pd in Pd−Rh nanocrystals was leached less (ca. 5−15%) into the solution. Thus, it seemed that Rh has played a significant role in not only tailoring the morphology but also enhancing the shape stability, probably resulting from the higher energy barrier to reconstruct the surface structure induced by incorporating inert Rh on the surfaces of Pd−Rh nanoparticles discussed by Kim et al.[25] Meanwhile, we examined the contribution of the homogeneous Pd leached into solution to the overall catalytic activity of the nanocatalysts (Figure S21). Our findings suggested that they contributed less than 20%, a small percentage compared to the amount of leached Pd, indicating that the differences in TOFs of various nanocatalysts did not result from the difficulty of Pd leaching but rather from the catalytic activity of Pd atoms on the surface of nanocrystals.

CONCLUSIONS

Pd−Rh nanocrystals with various morphologies and compositions could be obtained via a one-step hydrothermal method with finely regulated synthetic conditions. Pd−Rh hollow NCs with various compositions were formed through an iodine adsorbate-induced reconstruction mechanism by utilizing the etching effect with a mixture of a large amount of KBr and mere KI added. In the absence of KI, with slowing the growth rate of the NPs in order to manipulate nanocrystals in the growth mode within kinetic and thermodynamic regime, Pd−Rh NTOs with different Pd/Rh ratios were obtained when the amount of KBr was increased significantly. However, with controlling the nucleation of twinned seeds by adjusting the Pd/Rh ratio in the presence of a small portion of KBr, Pd−Rh NIs were eventually formed from the (111) twinned seeds as generated. Pd−Rh NPs with different compositions and shapes prepared in this work were further utilized as nanocatalysts for Suzuki cross-coupling reactions with various reactants, including inert and active ones. According to TOF results, morphology differences held more marked effects on catalytic activities compared to composition changes. Due to the presence of rich kink and step sites on the inner rough faces, Pd−Rh hollow NCs showed obviously enhanced catalytic activities with stability for Suzuki reactions compared to other

Pd-based solid NPs. In addition, Pd-based solid NCs, which were enclosed with (100) facets, held higher activity than other solid NPs with at least a part of (111) facets exposed. Meanwhile, for Suzuki reactions with more inert reactants, Pd−Rh hollow NCs showed relatively more enhanced catalytic activities, indicating their promising catalytic property for other Pd-catalyzed powerful methodologies. In summary, the systematic synthetic strategy of Pd−Rh nanocrsytals demonstrated in this work could be utilized to guide the tailoring and optimizing of metal nanostructures and could help in understanding the effects of morphology and composition in tuning their unique catalytic properties for wide applications.

ASSOCIATED CONTENT

Ⓢ Supporting Information

Additional TEM images, ICP-AES results, HAADF-STEM-EDS line-scan profiles, and other data are included. This material is available free of charge via the Internet at http://pubs.acs.org.

AUTHOR INFORMATION

Corresponding Author
*E-mail: ywzhang@pku.edu.cn.

Author Contributions
‡S.-B.W. and W.Z. contributed equally.

Notes
The authors declare no competing financial interest.

REFERENCES

(1) (a) Ruan, L.; Zhu, E.; Chen, Y.; Lin, Z.; Huang, X.; Duan, X.; Huang, Y. *Angew. Chem., Int. Ed.* **2013**, *52*, 12577−12581. (b) Oezaslan, M.; Hasché, F.; Strasser, P. *J. Phys. Chem. Lett.* **2013**, *4*, 3273−3291.

(2) (a) Mu, R.; Fu, Q.; Xu, H.; Zhang, H.; Huang, Y.; Jiang, Z.; Zhang, S.; Tan, D.; Bao, X. *J. Am. Chem. Soc.* **2011**, *133*, 1978−1986. (b) Iablokov, V.; Beaumont, S. K.; Alayoglu, S.; Pushkarev, V. V.; Specht, C.; Gao, J.; Alivisatos, A. P.; Kruse, N.; Somorjai, G. A. *Nano Lett.* **2012**, *12*, 3091−3096.

(3) (a) Jin, M.; Zhang, H.; Xie, Z.; Xia, Y. *Angew. Chem., Int. Ed.* **2011**, *50*, 7850−7854. (b) Wang, F.; Li, C.; Sun, L.-D.; Xu, C.-H.; Wang, J.; Yu, J. C.; Yan, C.-H. *Angew. Chem., Int. Ed.* **2012**, *51*, 4872−4876. (c) Scheuermann, G. M.; Rumi, L.; Steurer, P.; Bannwarth, W.; Mülhaupt, R. *J. Am. Chem. Soc.* **2009**, *131*, 8262−8270. (d) Wu, Y.; Cai, S.; Wang, D.; He, W.; Li, Y. *J. Am. Chem. Soc.* **2012**, *134*, 8975−8981. (e) Witham, C. A.; Huang, W.; Tsung, C.-K.; Kuhn, J. N.; Somorjai, G. A.; Toste, F. D. *Nat. Chem.* **2010**, *2*, 36−41.

(4) (a) Dasgupta, N. P.; Liu, C.; Andrews, S.; Prinz, F. B.; Yang, P. *J. Am. Chem. Soc.* **2013**, *135*, 12932−12935. (b) Guo, S.; Zhang, S.; Sun, S. *Angew. Chem., Int. Ed.* **2013**, *52*, 8526−8544.

(5) (a) Copéret, C.; Chabanas, M.; Saint-Arroman, R. P.; Basset, J.-M. *Angew. Chem., Int. Ed.* **2003**, *42*, 156−181. (b) Astruc, D.; Lu, F.; Aranzaes, J. R. *Angew. Chem., Int. Ed.* **2005**, *44*, 7852−7872. (c) Bäckvall, J.-E. *Top. Catal.* **2010**, *53*, 831−975. (d) Zaera, F.; Joyner, R. *Top. Catal.* **2008**, *48* (1-4), 1−168.

(6) (a) Phan, N. T. S.; Sluys, M. V. D.; Jones, C. W. *Adv. Synth. Catal.* **2006**, *348*, 609−679. (b) Miyaura, N.; Suzuki, A. *Chem. Rev.* **1995**, *95*, 2457−2483. (c) McGlacken, G. P.; Bateman, L. M. *Chem. Sov. Rev.* **2009**, *38*, 2447−2464. (d) Chen, X.; Engle, K. M.; Wang, D.-H.; Yu, J.-Q. *Angew. Chem., Int. Ed.* **2009**, *48*, 5094−5115.

(7) Ellis, P. J.; Fairlamb, I. J. S.; Hackett, S. F. J.; Wilson, K.; Lee, A. F. *Angew. Chem., Int. Ed.* **2010**, *49*, 1820−1824.

(8) (a) An, K.; Alayoglu, S.; Ewers, T.; Somorjai, G. A. *J. Colloid Interface Sci.* **2012**, *373*, 1−13. (b) Gao, F.; Goodman, D. W. *Chem. Sov. Rev.* **2012**, *41*, 8009−8020. (c) Xia, X.; Wang, Y.; Ruditskiy, A.; Xia, Y. *Adv. Mater.* **2013**, *25*, 6313−6333. (d) Hu, S.; Wang, X. *Chem. Sov. Rev.* **2013**, *42*, 5577−5594.

(9) (a) Gu, J.; Zhang, Y.-W.; Tao, F. *Chem. Sov. Rev.* **2012**, *41*, 8050−8065. (b) Wang, D.; Li, Y. *Adv. Mater.* **2011**, *23*, 1044−1060. (c) Yamada, Y.; Tsung, C.-K.; Huang, W.; Huo, Z.; Habas, S. E.; Soejima, T.; Aliaga, C. E.; Somorjai, G. A.; Yang, P. *Nat. Chem.* **2011**, *3*, 372−376. (d) Carpenter, M. K.; Moylan, T. E.; Kukreja, R. S.; Atwan, M. H.; Tessema, M. M. *J. Am. Chem. Soc.* **2012**, *134*, 8535−8542. (e) Lim, B.; Jiang, M.; Camargo, P. H. C.; Cho, E. C.; Tao, J.; Lu, X.; Zhu, Y.; Xia, Y. *Science* **2009**, *324*, 1302−1305. (f) Wu, Y.; Wang, D.; Niu, Z.; Chen, P.; Zhou, G.; Li, Y. *Angew. Chem., Int. Ed.* **2012**, *51*, 12524−12528.

(10) (a) Wang, L.; Yamauchi, Y. *Chem. Mater.* **2011**, *23*, 2457−2465. (b) Wu, Y.; Wang, D.; Chen, X.; Zhou, G.; Yu, R.; Li, Y. *J. Am. Chem. Soc.* **2013**, *135*, 12220−12223. (c) Zhu, H.; Zhang, S.; Guo, S.; Su, D.; Sun, S. *J. Am. Chem. Soc.* **2013**, *135*, 7130−7133.

(11) (a) Yin, A.-X.; Min, X.-Q.; Zhang, Y.-W.; Yan, C.-H. *J. Am. Chem. Soc.* **2011**, *133*, 3816−3819. (b) Lu, C.-L.; Prasad, K. S.; Wu, H.-L.; Ho, J-a. A.; Huang, M. H. *J. Am. Chem. Soc.* **2010**, *132*, 14546−14553. (c) Wang, L.; Yamauchi, Y. *J. Am. Chem. Soc.* **2013**, *135*, 16762−16765. (d) Wang, S.-B.; Zhu, W.; Ke, J.; Gu, J.; Yin, A.-X.; Zhang, Y.-W.; Yan, C.-H. *Chem. Commun.* **2013**, *49*, 7168−7170. (e) Huang, X.; Zhang, H.; Guo, C.; Zhou, Z.; Zheng, N. *Angew. Chem., Int. Ed.* **2009**, *48*, 4808−4812. (f) Saleem, F.; Zhang, Z.; Xu, B.; Xu, X.; He, P.; Wang, X. *J. Am. Chem. Soc.* **2013**, *135*, 18304−18307.

(12) (a) Strasser, P.; Koh, S.; Anniyev, T.; Greeley, J.; More, K.; Yu, C.; Liu, Z.; Kaya, S.; Nordlund, D.; Ogasawara, H.; Toney, M. F.; Nilsson, A. *Nat. Chem.* **2010**, *2*, 454−460. (b) Liu, Y.; Chi, M.; Mazumder, V.; More, K. L.; Soled, S.; Henao, J. D.; Sun, S. *Chem. Mater.* **2011**, *23*, 4199−4203.

(13) (a) Kobayashi, H.; Morita, H.; Yamauchi, M.; Ikeda, R.; Kitagawa, H.; Kubota, Y.; Kato, K.; Takata, M.; Toh, S.; Matsumura, S. *J. Am. Chem. Soc.* **2012**, *134*, 12390−12393. (b) Yoon, B.; Pan, H.-B.; Wai, C. M. *J. Phys. Chem. C* **2009**, *113*, 1520−1525. (c) Renzas, J. R.; Huang, W.; Zhang, Y.; Grass, M. E.; Hoang, D. T.; Alayoglu, S.; Butcher, D. R.; Tao, F.; Liu, Z.; Somorjai, G. A. *Phys. Chem. Chem. Phys.* **2011**, *13*, 2556−2562.

(14) (a) Xie, S.; Peng, H.-C.; Lu, N.; Wang, J.; Kim, M. J.; Xie, Z.; Xia, Y. *J. Am. Chem. Soc.* **2013**, *135*, 16658−16667. (b) Xie, S.; Lu, N.; Xie, Z.; Wang, J.; Kim, M. J.; Xia, Y. *Angew. Chem., Int. Ed.* **2012**, *51*, 10266−10270. (c) Sneed, B. T.; Brodsky, C. N.; Kuo, C.-H.; Lamontagne, L. K.; Jiang, Y.; Wang, Y.; Tao, F.; Huang, W.; Tsung, C.-K. *J. Am. Chem. Soc.* **2013**, *135*, 14691−14700. (d) Sneed, B. T.; Kuo, C.-H.; Brodsky, C. N.; Tsung, C.-K. *J. Am. Chem. Soc.* **2012**, *134*, 18417−18426.

(15) Reyes-Gasga, J.; Tehuacanero-Nuñez, S.; Montejano-Carrizales, J. M.; Gao, X.; Jose-Yacaman, M. *Top. Catal.* **2007**, *46*, 23−30.

(16) Ding, Y.; Fan, F.; Tian, Z.; Wang, Z. L. *J. Am. Chem. Soc.* **2010**, *132*, 12480−12486.

(17) (a) Peng, H.-C.; Xie, S.; Park, J.; Xia, X.; Xia, Y. *J. Am. Chem. Soc.* **2013**, *135*, 3780−3783. (b) Zhang, Y.; Grass, M. E.; Kuhn, J. N.; Tao, F.; Habas, S. E.; Huang, W.; Yang, P.; Somorjai, G. A. *J. Am. Chem. Soc.* **2008**, *130*, 5868−5869.

(18) (a) Schimpf, J. A.; McBride, J. R.; Soriaga, M. P. *J. Phys. Chem.* **1993**, *97*, 10518−10520. (b) Kim, Y.-G.; Baricuatro, J. H.; Soriaga, M. P.; Suggs, D. W. *J. Electroanal. Chem.* **2001**, *509*, 170−174.

(19) Wiley, B.; Herricks, T.; Sun, Y.; Xia, Y. *Nano Lett.* **2004**, *4*, 1733−1739.

(20) (a) Srivastava, S. C.; Newman, L. *Inorg. Chem.* **1966**, *5*, 1506−1510. (b) Feldberg, S.; Klotz, P.; Newman, L. *Inorg. Chem.* **1972**, *11*, 2860−2865. (c) Zhu, C.; Zeng, J.; Lu, P.; Liu, J.; Gu, Z.; Xia, Y. *Chem.—Eur. J.* **2013**, *19*, 5127−5133.

(21) (a) Wang, Z. L. *J. Phys. Chem. B* **2000**, *104*, 1153−1175. (b) Xia, X.; Xie, S.; Liu, M.; Peng, H.-C.; Lu, N.; Wang, J.; Kim, M. J.; Xia, Y. *Proc. Natl. Acad. Sci. U.S.A.* **2013**, *110*, 6669−6673.

(22) Zhang, Q.; Xu, J.; Yan, D.; Li, S.; Lu, J.; Cao, X.; Wang, B. *Catal. Sci. Technol.* **2013**, *3*, 2016−2024.

(23) Yin, A.-X.; Min, X.-Q.; Zhu, W.; Wu, H.-S.; Zhang, Y.-W.; Yan, C.-H. *Chem. Commun.* **2012**, *48*, 543−545.

(24) Pagliaro, M.; Pandarus, V.; Ciriminna, R.; Béland, F.; Carà, P. D. *ChemCatChem* **2012**, *4*, 432−445.

(25) Lu, N.; Wang, J.; Xie, S.; Xia, Y.; Kim, M. J. *Chem. Commun.* **2013**, *49*, 11806−11808.